OPTICA

High-speed, low-voltage, low-bit-energy silicon photonic crystal slow-light modulator with impedance-engineered distributed electrodes

Keisuke Kawahara,[1,*] Tai Tsuchizawa,[2] Noritsugu Yamamoto,[2] Yuriko Maegami,[2] Koji Yamada,[2] Shinsuke Hara,[3] and Toshihiko Baba[1]

[1]Department of Electrical and Computer Engineering, Yokohama National University, Yokohama, 240-8501, Japan
[2]National Institute of Advanced Industrial Science and Technology (AIST), Tsukuba, 305-8568, Japan
[3]National Institute of Information and Communications Technology (NICT), Koganei, 184-8795, Japan
*keisuke@ieee.org

Received 28 May 2024; revised 5 August 2024; accepted 8 August 2024; published 28 August 2024

Silicon modulators in optical transceivers feature high-density integration and low manufacturing cost, but they also need to deliver high speed and low power consumption to meet the demands of future data centers and high-performance computing. This paper demonstrates a significantly improved 64 Gbps silicon Mach–Zehnder modulator incorporating photonic crystal slow-light phase shifters. By employing distributed electrodes and engineering their impedance, electro-optic phase matching and electrical impedance matching were obtained simultaneously, and the driving voltage was reduced to 0.87 V, which is compatible with fin-type field effect transistors and eliminates the need for additional electrical amplifiers. The bit energy of as low as 59 fJ/bit is comparable to that of microring modulators, while this modulator does not require temperature control like that used for microring modulators, due to its wide working spectrum of 6 nm. These results indicate the potential for addressing power issues in next-generation data infrastructures. © 2024 Optica Publishing Group under the terms of the Optica Open Access Publishing Agreement

https://doi.org/10.1364/OPTICA.531372

1. INTRODUCTION

Artificial intelligence and internet of things have swiftly increased the demand for data centers and high-performance computers [1,2]. Optical interconnects are used for reducing energy loss in electrical wiring [3,4]. Silicon (Si) photonics is a powerful photonic integration platform for optical interconnects due to its compatibility with the mature electronic process [5]. Si optical modulators in optical transceivers possess advantages such as high speed, small footprint, and low manufacturing cost [6–14]. To address future power saving issues, Si modulators must achieve high speed and low power consumption simultaneously [15,16]. Microring modulators (MRMs) attain a small footprint and a bit energy as low as a few tens of fJ/bit at a resonance wavelength [17–20]. However, the external temperature control to suppress resonance drift increases the total power consumption [12–14]. By contrast, Mach–Zehnder modulators (MZMs) operate over the broad wavelength range, rendering temperature control unnecessary, but their long phase shifters necessitate a bit energy of several pJ/bit [21–26]. To enhance power efficiency, the heterogeneous integration of materials such as III–V semiconductors [27,28], polymers [29,30], graphene [31,32], and lithium niobate [33–36] have been investigated. However, such integration needs complex manufacturing processes that are incompatible with standard complementary metal oxide semiconductor (CMOS) technology.

A vital research question is whether Si MZMs can reduce the bit energy with structural innovations that do not entail process changes. Photonic crystal waveguides (PCWs) demonstrate slow light with a low group velocity, which enhances any optical effects [37]. Slow light lessens $V_\pi L$ in proportion to the group index n_g and lowers the length and capacitance C_{pn} of the phase shifters [38]. When applying slow light to high-speed MZMs, however, electro-optic phase matching must be addressed even for short phase shifters, because the group velocities of slow light and RF signals are much more different than in usual MZMs. For this purpose, meanderline RF electrodes were inserted into traveling-wave electrodes in the PCW slow-light MZM as electrical delay lines, and the operation up to 64 Gbps has been demonstrated [39,40]. But still the driving voltage V_{pp} was as high as 3.5–5.2 V, which cannot be supplied by a fin-type field effect transistor (FinFET), necessitating the addition of electrical amplifiers.

Related with this, the reduction in bit energy is another crucial issue. In the previous reports, to evaluate the modulation capability of the phase shifter, the bit energy was estimated from the charge energy $C_{pn}V_{pp}^2/2$ accumulated in the p-n junction and partly dissipated by the junction resistance R_{pn}. However, the practical power consumption in a traveling-wave MZM is rather dominated by the termination resistor R_T. It is easily understood when R_{pn} is negligible, and no power dissipation occurs in the p-n junction. The result is almost the same if R_{pn} is non-negligible; although

some RF power is lost at the junction, the remaining power ends up being dissipated in R_T. From the practical power consumption $V_{pp}^2/4R_T$, the bit energy of the previous slow-light MZMs is calculated to be 200, 625, and 2,400 fJ/bit at bitrates of 25, 32, and 64 Gbps, respectively [39,40]. The high bit energy at 64 Gbps is due to the high driving voltage and a low R_T of 20 Ω employed to improve high-frequency response. This bit energy can be reduced by increasing R_T, but to achieve impedance matching, the characteristic impedance Z_0 of the electrodes must also be increased. If the parasitic resistance is small, Z_0 is approximated by $\sqrt{(L/C_{pn})}$. To increase the inductance component L, distributed electrodes using spiral inductors were introduced into a rib-type MZM [41]. However, C_{pn} of the rib-type phase shifters is very large, so large inductors are necessary to obtain a high Z_0, which results in a large footprint and RF loss, limiting the bandwidth to less than 20 GHz. On the other hand, applying this concept to the slow-light MZM, a high Z_0 can be achieved by small C_{pn} of the shortened phase shifter and the electrode inductance of a reasonable length, although such consideration has not yet been taken for previous MZMs.

In this study, we engineered the impedance of the distributed electrodes in the slow-light MZM so that the electro-optic phase matching and impedance matching were simultaneously achieved. In this paper, we present the details of its design, fabrication, and demonstration at 64 Gbps. We finally conclude that this device is a promising candidate for balancing high speed, low voltage, low bit energy, small footprint, and temperature-control-free operation.

2. DEVICE STRUCTURE

Figures 1(a) and 1(b) show the schematic of the distributed electrode Si PCW slow-light MZM and a circuit model of the electrode. The p-n doped phase shifter is divided into N segments of l_{seg} length. The phase shifter operates with a reverse bias in the carrier depletion mode to avoid bandwidth limitation due to carrier transience. The wiring inductors L_H are inserted between the segmented phase shifters to form an LC ladder like a distributed constant circuit. The wiring inductance of a coplanar waveguide with a characteristic impedance of $Z_H > Z_0$ and a phase constant of β_H was used for L_H. When l_{seg} is sufficiently shorter than the RF wavelength λ_{RF}, the phase shifter is modeled as a lumped RC series circuit. Figure 1(c) shows a lumped π model of the coplanar waveguide with a length of $l_m \ll \lambda_{RF}$. The series inductor and shunt capacitor are approximated by $L_H = Z_H\beta_H l_m/\omega$ and $C_H = \beta_H l_m/\omega Z_H$, respectively. Then, the unit cell of the electrode is modeled as a symmetric T-shaped network shown in Fig. 1(d). Assuming $\omega R_{pn} C_{pn} \ll 1$, Z_0 is approximated by

$$Z_0 \approx \sqrt{\frac{L_H}{C_H + C_{pn}}}. \tag{1}$$

Figure 1(e) shows the simulated Z_0, which is increased from 35 Ω to 52 Ω with the inductors. The RF power propagates through the electrodes while being dissipated by R_{pn}, which can limit the bandwidth. The RF propagation constant $\alpha_{RF} + j\beta_{RF}$ is approximated by

$$\alpha_{RF} + j\beta_{RF} \approx \frac{1}{l_U}\left(\frac{\omega^2 R_{pn} C_{pn}^2 Z_0}{2} + j\omega\sqrt{L_H\left(C_H + C_{pn}\right)}\right), \tag{2}$$

where l_U is the unit cell length (see Supplement 1 for detailed derivation). Assuming that the roll-off due to phase mismatch is sufficiently small, the normalized electro-optic frequency response $G_{EO}(f)$ is determined by the RC response $G_{RC}(f)$ and the mean propagation loss for each segment, as follows:

$$\begin{aligned} G_{EO}(f) &= G_{RC}(f) \cdot \frac{1}{N}\sum_{n=1}^{N} e^{-(n-1)\alpha_{RF} l_U} \\ &= \left|\frac{1}{1 + j\omega R_{pn} C_{pn}}\right| \cdot \frac{1 - e^{-N\alpha_{RF} l_U}}{N\left(1 - e^{-\alpha_{RF} l_U}\right)}. \end{aligned} \tag{3}$$

Figures 1(f) and 1(g) show the calculated total electrode length and EO bandwidth $f_{3\,dB}$ required to achieve $Z_0 = 50\,\Omega$. As n_g increases, electrodes required for high impedance become shorter, reducing RF losses. Thus, the combination of slow light and distributed electrodes allows for high impedance while preserving a wide bandwidth, leading to a low bit energy. At sufficiently high n_g, the $f_{3\,dB}$ approaches the intrinsic RC limitation of the phase shifter. However, the PCW working spectrum also narrows. To achieve an optimal balance between a sufficient EO bandwidth and a sufficient working spectrum, we chose $n_g = 20$.

Another advantage of distributed electrodes is the phase matching between the slow light and the RF signal, as already demonstrated by the previous meanderline electrode [39]. In distributed electrodes of this study, a greater N facilitates more rigorous phase matching and greater sinc roll-off frequencies. The phase shift per unit cell is given by $\theta_U(\omega) = \beta_{RF} l_U$. Figures 2(a) and 2(b) present the simulated frequency response of the electro-optic conversion gain and the group delay for the standard and distributed electrodes. This simulation was performed by using Keysight's Advanced Design System circuit simulator and in-house photonic device models. The models include electro-optic phase mismatch, RC time constant, and RF propagation loss as bandwidth-restricting factors. The simulations performed agree with the measurements of at least up to 40 GHz [42]. Similar to the meanderline electrode, the distributed electrode successfully suppresses the sinc roll-off, leading to a broadband response with $f_{3dB} = 39$ GHz. The simulated f_{3dB} is slightly lower than the calculated value in Fig. 1(g) due to additional RF losses at the series parasitic resistance in the wiring but is sufficient for digital signal processing (DSP)-free 64-Gbaud signal transmission. This modulator's primary bandwidth-restricting influence is the RC time constant of the p-n junction, and the frequency response demonstrates a slow roll-off that can be assessed as a first-order lag element. The bandwidth can be increased further by applying a simple linear equalizer, owing to the slow roll-off. As an example, with only 1.3 dB of DC suppression, f_{3dB} can be up to 50 GHz and can transmit 100-Gbaud signals. This property highlights the potential application of the proposed MZM in future optical interconnects. Moreover, the group delay ripple is within ±1 ps up to 40 GHz thanks to the strict impedance matching. This flat group delay response reduces the jitter and improves eye opening. An important feature of the distributed electrodes is that the impedance and phase delay are completely independent. The electrode design parameters (Z_H and l_m) can be uniquely determined to simultaneously satisfy the impedance matching and EO phase matching requirements. A more detailed analysis and design guidelines are presented in Section 2 of Supplement 1.

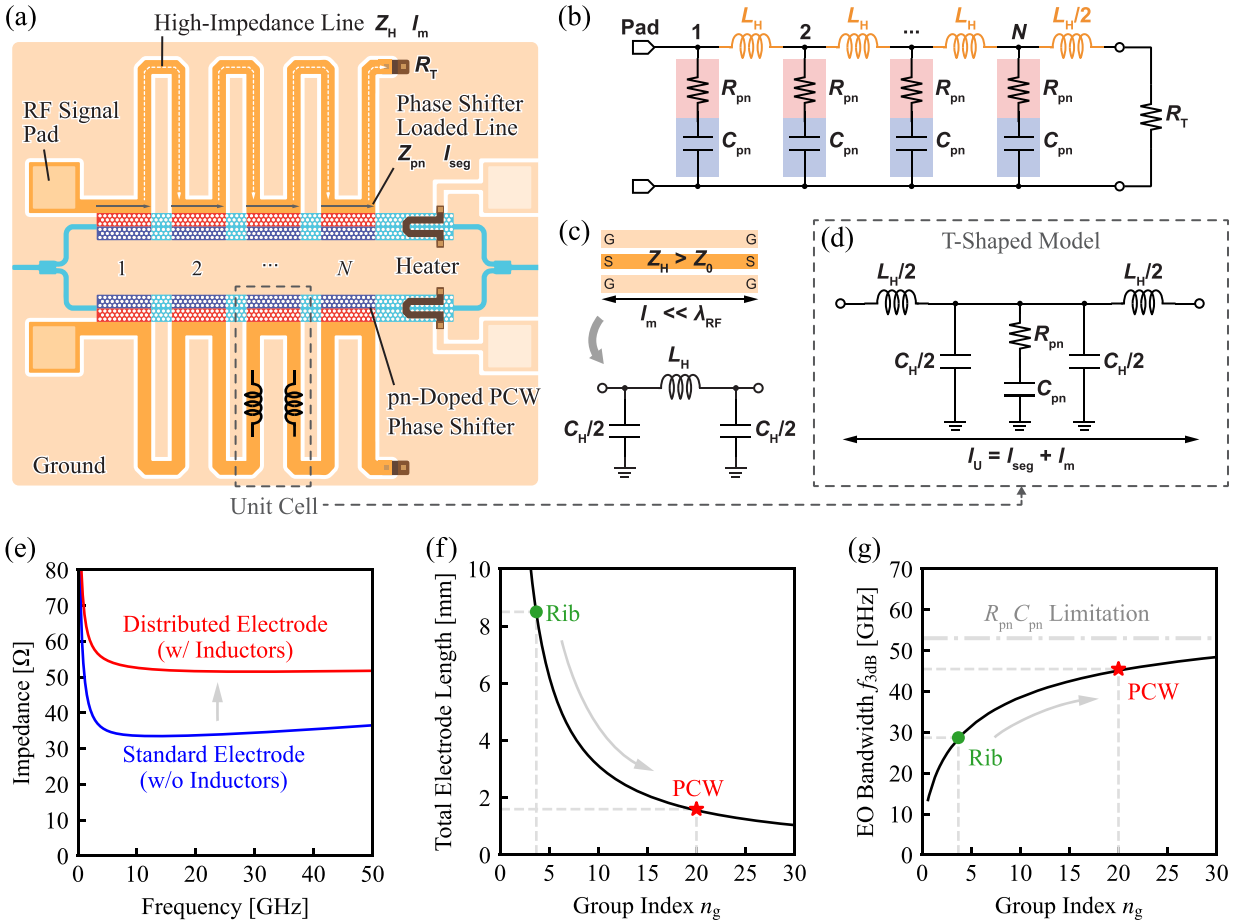


Fig. 1. Distributed electrode Si PCW slow-light MZM. (a) Schematic. (b) Circuit model of the electrode. (c) Lumped π model of the coplanar waveguide. (d) Circuit model of the unit cell. (e) Simulated characteristic impedance Z_0 with and without inductors at $l_m = 470$ μm, $l_{seg} = 50$ μm, $Z_H = 55$ Ω, $R_{pn} \cdot l_{seg} = 12$ Ω · mm, and $C_{pn}/l_{seg} = 250$ fF/mm. (f) Calculated total electrode length to achieve $Z_0 = 50$ Ω. (g) Achievable $f_{3\,dB}$ at $Z_0 = 50$ Ω.

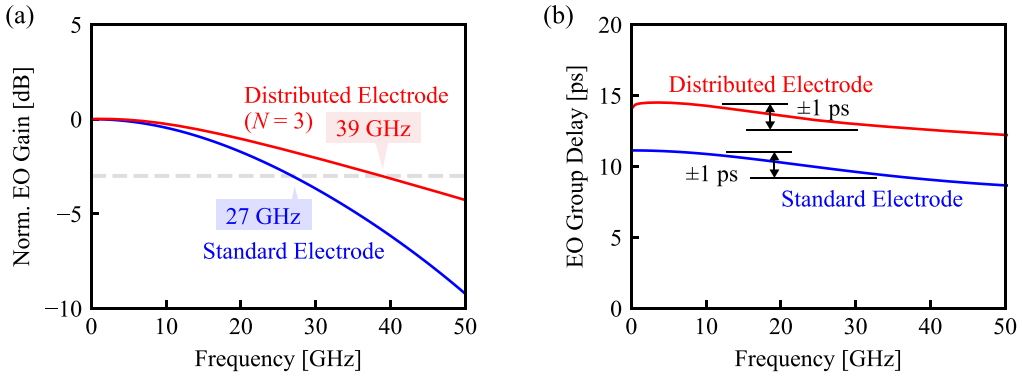


Fig. 2. Simulated frequency responses. (a) Normalized electro-optic conversion gain. (b) Group delay.

These structural advantages of the proposed MZM can be applied to other material platforms if their phase shifter is shortened and the junction capacitance is reduced, e.g., by the slow-light effect. The inductance of the electrode required to obtain a high impedance is comparably reduced, resulting in a practically small footprint and low RF losses. For example, a thin-film lithium niobate (TFLN) MZM with slow-light enhancement has recently been reported [43]. TFLN MZMs require a smaller electrode gap to obtain smaller V_π, as well as impedance matching, phase matching, and low RF loss [44]. Applying electrode engineering, as done in this study, to TFLN slow-light MZMs will help overcome these trade-offs.

3. RESULTS AND DISCUSSION

A. Device Fabrication

Figure 3(a) shows a prototype device fabricated in a CMOS-compatible 300-mm Si-on-insulator process. Its footprint was only 0.5 mm × 0.6 mm = 0.3 mm^2 including electrodes. The wire width and gap of the coplanar waveguide were set to 8 and 6 μm,

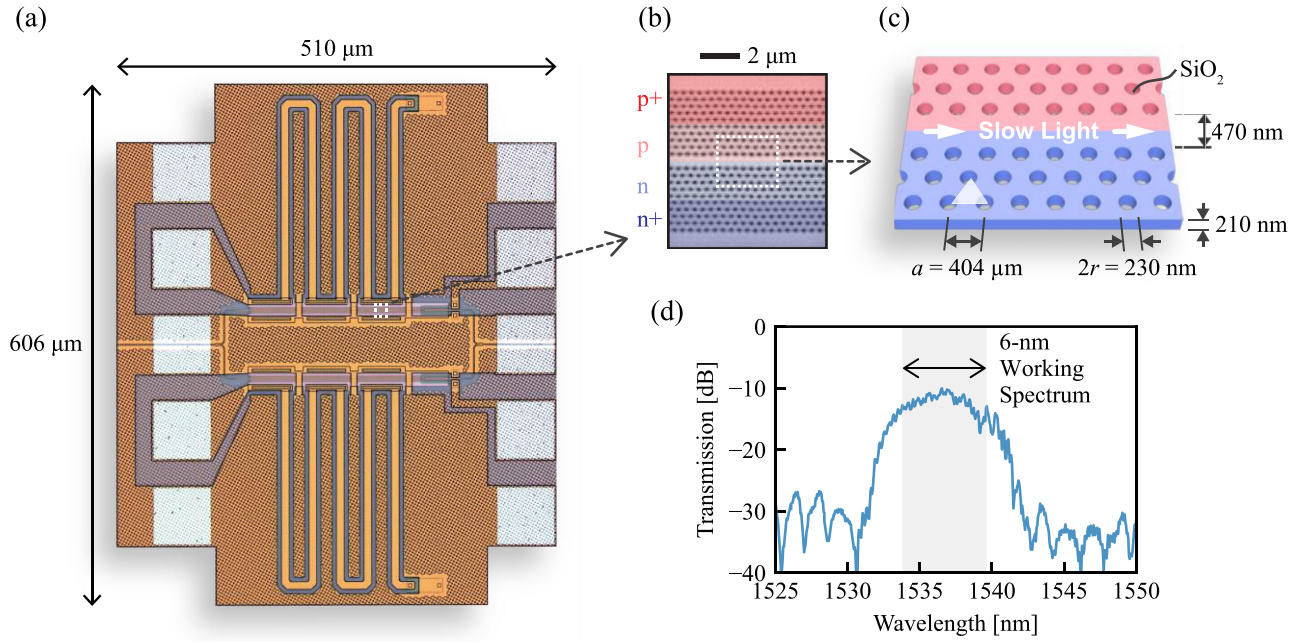


Fig. 3. Developed Si PCW slow-light MZM. (a) Micrograph. (b) Laser micrograph of the phase shifter. (c) Schematic structure of the PCW. (d) Measured optical transmission spectrum of the MZM.

respectively, through electromagnetic field analysis to achieve $Z_H = 55\ \Omega$. The Si dummy was blocked just below the coplanar waveguide to suppress the high-frequency losses (Supplement 1). Figures 3(b) and 3(c) show a magnified view and schematic of the PCW phase shifter. The lattice constant was set to $a = 404$ nm, and the hole diameter was $d = 230$ nm to attain a C-band photonic bandgap. The p- and n-type doping concentrations were set to $N_A = 9.5 \times 10^{17}\ \mathrm{cm}^{-3}$ and $N_D = 1.0 \times 10^{18}\ \mathrm{cm}^{-3}$, respectively, to achieve balance between the optical loss and the modulation efficiency. The bottom of the electrode contacts was highly doped to attain an excellent ohmic junction. Figure 3(d) demonstrates the measured optical transmission spectrum of the device. The intrinsic losses in the measurement setup were removed by normalizing the measured spectrum to that of a reference Si waveguide. The total insertion loss was approximately 10 dB, including those at the multi-mode interference couplers of ∼0.5 dB × 2, the transition between the Si waveguide and PCW of ∼0.4 dB × 2, bends of ∼0.03 dB × 6, and the p-n doped PCW phase shifter of ∼8 dB. The slab thickness was decreased slightly, depending on process variations, which slightly raised the optical loss and moved the spectral window toward shorter wavelengths. Nevertheless, the 6-nm spectrum window was sufficiently wide to eliminate the temperature compensation. The full C-band can be covered under a constant n_g by employing lattice-shifted PCWs demonstrated beforehand [45]. In the future, the loss is expected to be reduced by optimizing doping profiles [46] and component structures [47], and investigating new materials [43]. The prototype device exhibited $n_g \approx 30$ at the wavelength used in the modulation experiments described below, which is higher than targeted $n_g = 20$ due to variations in slab thickness (see Section 5 of Supplement 1). This variation caused EO phase mismatch, narrowing the bandwidth to $f_{3dB} \approx 31$ GHz, but still maintaining 64-Gbaud modulation capability.

B. Impedance

The impedance of the distributed electrode was assessed using a setup in Fig. 4(a). The S-parameters were measured using a Keysight PNA-X N5247B vector network analyzer calibrated by the line-reflect-reflect-match method at the probe tip. The measured S-parameters were de-embedded to remove the pad capacitance, ensuring consistency with the simulation. A DC bias voltage of $V_{DC} = -2$ V was applied to the device via a bias-T. Figure 4(b) presents the measured and simulated reflection coefficients. The measurement results were roughly consistent with the simulation. The deviation between the simulation and the measurement was due to model errors in the electromagnetic field analysis. The reflection was less than −18 dB at all frequencies, and satisfactory broadband matching was attained for the 50-Ω reference impedance. Figure 4(c) exhibits the real and imaginary parts of the input impedance. The resistive and reactive components were almost 50 and 0 Ω, respectively, over the measured frequency range of up to 60 GHz. This frequency-independent high impedance decreased power consumption while sustaining an excellent signal quality and lowering the bit energy.

C. Back-to-Back Signal Transmission

The transmission performance of the prototype device was experimentally assessed. A continuous-wave tunable laser was used as the light source, and the bias of the Mach–Zehnder interferometer was corrected to the quadrature point (quad. bias) or 5 dB deeper from the quadrature point (deep bias). A pulse pattern generator (PPG) and multiplexer produced a 50- or 64-Gbps nonreturn-to-zero (NRZ) signal. The device was push-pull driven by a broadband amplifier with $V_{pp} = 0.87$, 1.6, and 2.2 V. The first two voltages are compatible with the core and IO voltages of a 12-nm FinFET CMOS process [48]. The received signals were monitored using a

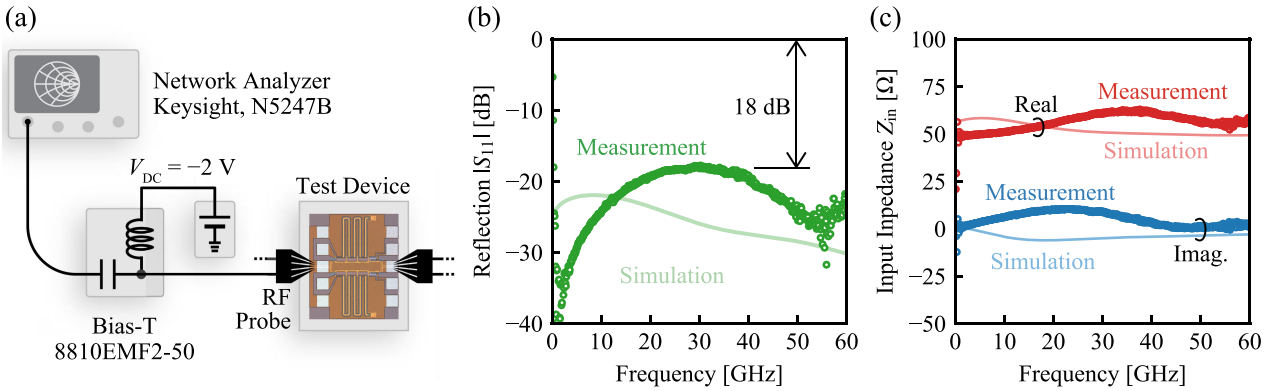


Fig. 4. Impedance measurement. (a) Setup. (b) Reflection coefficient for a reference impedance of 50 Ω. (c) Real and imaginary parts of the input impedance.

sampling oscilloscope and equalized using a five-tap linear equalizer in offline DSP. The experimental details are presented in Appendix A.

Figure 5(a) exhibits the DSP-free 50-Gbaud eye diagrams and the anticipated bit error rates (BERs). The dynamic extinction ratios (ERs) were 2.0 and 4.5 dB for quad. and deep bias at a driving voltage of 2.2 V, respectively. The modulation losses under the quad. and deep bias conditions were 2.1 dB and 6.3 dB, respectively. Observations reveal 50-Gbps DSP-free clear eye-opening with $V_{pp} < 1$ V for quad. and deep biases. The RF signal power

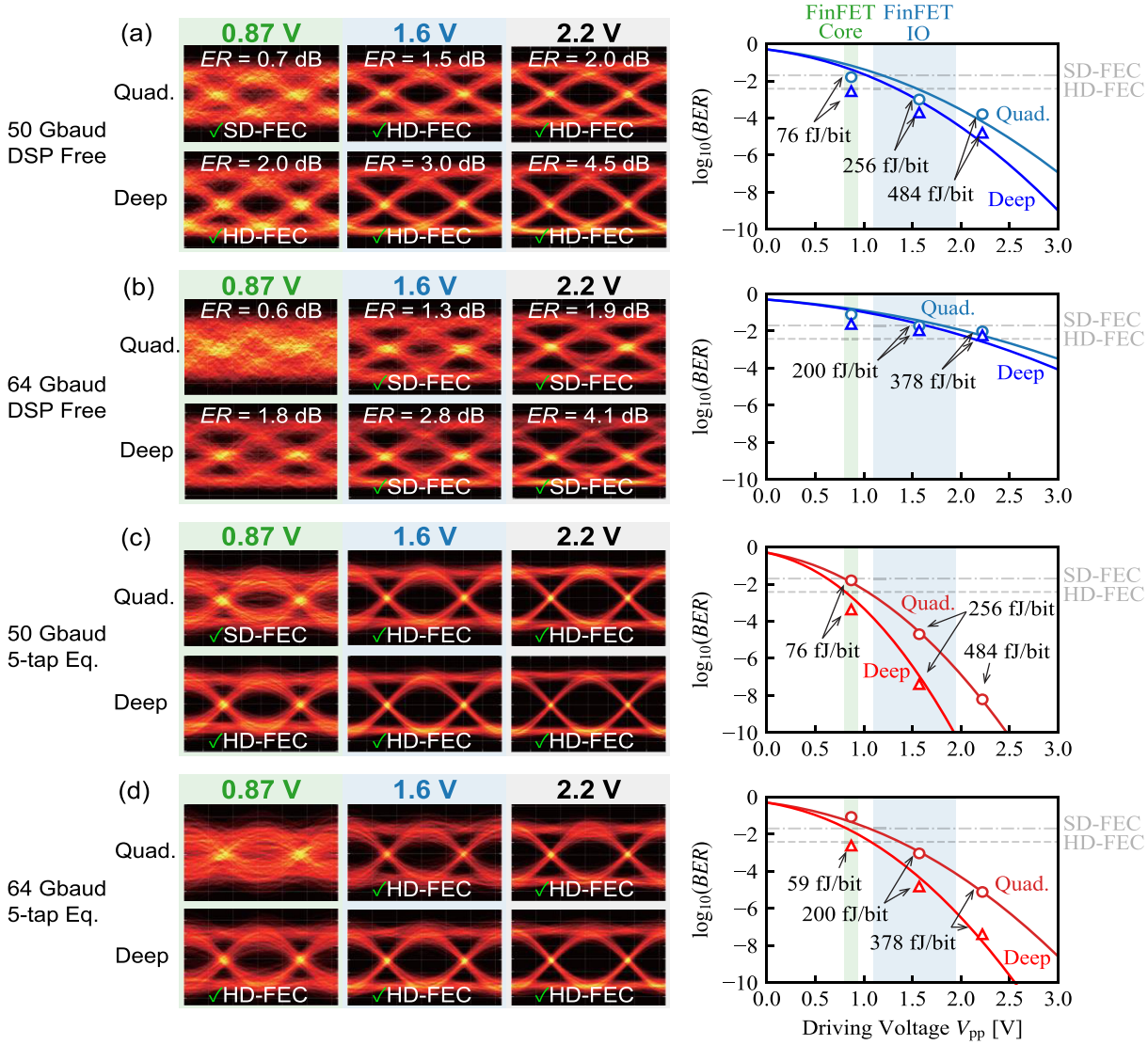


Fig. 5. Back-to-back signal transmission results under various driving voltages. (a) 50-Gbaud and (b) 64-Gbaud DSP-free eye diagrams and estimated BER. (c) 50-Gbaud and (d) 64-Gbaud equalizer eye diagrams and estimated BER using a five-tap adaptive linear equalizer.

consumptions were only 3.8, 13, and 24 mW at $V_{pp} = 0.87$, 1.6, and 2.2 V, respectively. In spite of the low power consumption, the projected BER fulfilled the forward error correction (FEC) threshold at all driving voltages. The high-impedance electrode successfully lowered the driving current, and the bit energies reached 76, 256, and 484 fJ/bit, respectively. These results are much lower than several pJ/bit of the standard Si MZMs. Figure 5(b) presents the DSP-free 64-Gbaud eye diagrams and estimated BER. The eye-opening was faintly degraded at 64 Gbaud, but the received signals still satisfied the soft decision (SD)-FEC threshold at $V_{pp} > 1.5$ V. Figures 5(c) and 5(d) exhibit the 50- and 64-Gbaud eye diagrams applying a five-tap linear equalizer. The signal quality was substantially enhanced with a simple linear equalizer owing to the slow roll-off response as expected by simulation. The device effectively transmitted 64-Gbps signals at $V_{pp} = 0.87$ V, exhibiting excellent FinFET compatibility, and a bit energy amounting to 59 fJ/bit.

Table 1 summarizes recent advancements in CMOS-compatible Si modulators. To estimate the modulation efficiency of our device, $V_\pi L$, we performed 2.4-Gbps modulation experiments at a high driving voltage of $V_{pp} = 3.17$ V to minimize the roll-off and noise. The device was driven directly by the PPG and biased at the quadrature point. We measured ER = 4.19 dB, and $V_\pi L$ was estimated to be 0.32 V·cm per phase shifter or 0.16 V·cm for push-pull drive. The DC $V_\pi L$ might be smaller than this value, considering the roll-off due to the high-frequency response. In our previous experiment [40], DC $V_\pi L$ of 0.44 V · cm per phase shifter was measured at $n_g = 20$. Therefore, the above value is reasonable given $n_g = 30$ of the prototype device. Traditionally, MZMs operating above 50 Gbps required smaller R_T [25,50,51]. Previous studies using 50-Ω terminations faced significant limitations in bitrate [41,54,55,57]. Single-drive structures resulted in a driving voltage at or above 5 V and bit energy exceeding 1.5 pJ/bit [21,26,54]. This study has demonstrated bit energy of less than 100 fJ/bit at 64 Gbps, which has overcome the trade-off between the efficiency and bitrate, as shown in Fig. 6. The bit energy approached that of MRMs while having a working spectrum of 6 nm, which is much wider than the typical sub-1-nm range of MRMs [18,19].

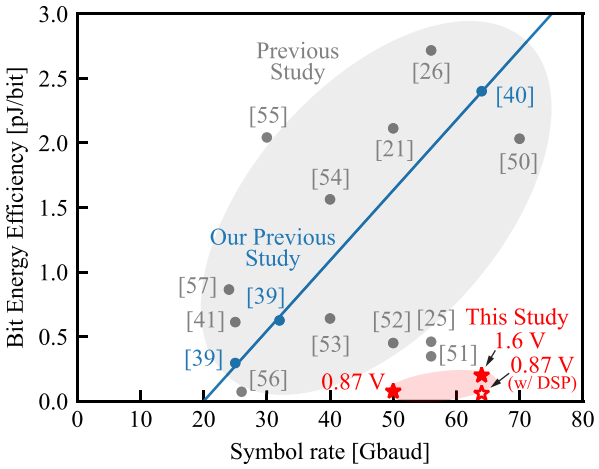


Fig. 6. Comparison of bit energy between this study and previous studies.

4. CONCLUSION

In this paper, 64-Gbps back-to-back signal transmission at a low driving voltage of less than 1 V was demonstrated using Si PCW slow-light MZMs. The distributed electrodes simultaneously achieved 50-Ω impedance and electro-optic phase matching, moderately suppressing RF losses. This approach highlighted the possible power advantages of the Si slow-light MZM, achieving a bit energy of 59 fJ/bit. The wide operating bandwidth of 6 nm removed the need for temperature control, thereby enhancing the overall system power performance. Furthermore, the device

Table 1. Comparison with the Previous CMOS-Compatible Modulators[a]

Reference	Type	Phase Shifter	$V_\pi L$ [V·cm]	Phase Shifter Loss [dB]	Symbol Rate [Gbaud]	V_{pp} [V]	R_T [Ω]	Efficiency [fJ/bit]
This study	**MZM**	**PCW**	**0.32 (small signal)**	**8**	**50, 64 (NRZ)**	**0.87**	**50**	**76, 59**
[40]	MZM	PCW	0.44	4	64 (NRZ)	3.5	20	2400
[39]	MZM	PCW	0.44	4	32, 25 (NRZ)	2, 1	50	625, 295
[49]	MZM	Bragg grating	0.96	5.4	112 (NRZ)	5	N.R.	N.R.
[50]	MZM	Rib	2.2–2.4	2.3	70 (NRZ)	3.2	18	2032
[51]	MZM	Rib	2.46	3	56 (NRZ)	1.65	35	347
[25]	MZM	Rib	1.4	4.4	56 (PAM4)	3.8 (single)	35	460
[26]	MZM	Rib	1.1	8	56 (NRZ)	7.8 (single)	50	2716
[21]	MZM	Rib	2.8	3.2	50 (NRZ)	6.5 (single)	50	2113
[52]	MZM	Rib	2.43–2.64	3.34	50 (NRZ)	1.5	25	450
[53]	MZM	Rib	2.43	3.6	40 (NRZ)	1.6	25	640
[54]	MZM	Bragg grating	0.6	–	40 (NRZ)	5 (single)	50	1563
[55]	MZM	Bragg grating	0.18	2	30 (NRZ)	3.5	50	2042
[56]	MZM	Rib	1.28	4.5	26 (NRZ)	0.5	33	72.8
[41]	MZM	Rib	0.9–1.4	2.7	25 (NRZ)	1.75	50	612
[57]	MZM	Rib	0.94 ($V_{DC} = -2$ V)	2.5	24 (NRZ)	2.88 (single)	50	864
[18]	MRM	Rib	0.52	–	64 (PAM4)	2.4 (single)	–	18
[19]	MRM	Rib	0.56–0.92	–	50 (PAM4)	1.5 (single)	–	14

[a]MZM, Mach–Zehnder modulator; MRM, microring modulator.

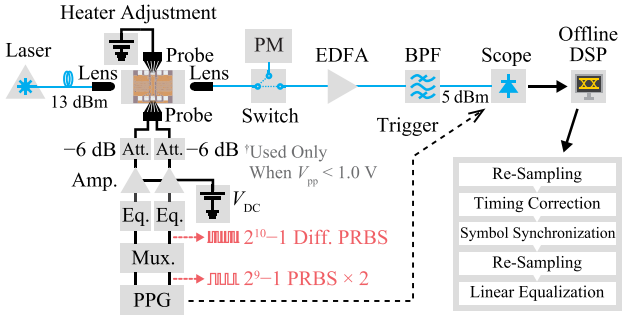


Fig. 7. Measurement setup for the back-to-back signal transmission experiment.

footprint was decreased to 0.3 mm^2 while retaining the CMOS process compatibility. The structural gains of the proposed MZM can be applied to other material platforms, and additional performance enhancements are also anticipated. These results mean that Si slow-light MZMs help to solve power problems in future data centers and high-performance computing.

APPENDIX A: EXPERIMENTAL DETAILS

Figure 7 exhibits the measurement setup employed for the back-to-back signal transmission experiment. A continuous-wave laser light with a power of 13 dBm was generated from Santec's TSL-550 tunable laser source. Two pseudorandom bit sequences were output from Anritsu's MP1800A PPG, and SHF's 601A multiplexer produced 50- or 64-Gbaud NRZ signals. SHF's EQ25A passive equalizer compensated for the RF cable losses. SHF's S804B driver expanded the electrical signal. A 6-dB attenuator was used to attain a CMOS-compatible driving voltage. The bias point of the modulation was set to the quadrature point and 5 dB deeper from the quadrature point by employing an on-chip TiN heater. The p-n junction of the phase shifter was biased to $V_{DC} = -1$ V when $V_{pp} < 1$ V and $V_{DC} = -2$ V otherwise. The generated light at the device was amplified using an erbium doped fiber amplifier, and the expanded spontaneous emission noise was removed using a bandpass filter with a bandwidth of 1 nm. The modulated optical signal was received by Keysight's 86100C sampling oscilloscope and 86116C photodetection module. The received waveforms were imported into MATLAB/Simulink for offline digital signal processing. The waveform was oversampled, and timing correction was applied to remove the intrinsic time distortion in the sampling oscilloscope. Then, the symbols were synchronized and resampled at the decision point. A symbol-by-symbol five-tap adaptive linear equalizer was employed to shape the waveform. The constant modulus algorithm determined the tap coefficients of the equalizer. The bit error rate was approximated by fitting a vertical histogram of the received signal with two Gaussian functions.

Funding. Japan Society for the Promotion of Science (JP23KJ0988).

Acknowledgment. This work was supported through the activities of VDEC, The University of Tokyo, in collaboration with Cadence Design Systems, Inc. and Keysight Technologies, Inc.

Disclosures. The authors declare no conflicts of interest.

Data availability. Data underlying the results presented in this paper are not publicly available at this time but may be obtained from the authors upon reasonable request.

Supplemental document. See Supplement 1 for supporting content.

REFERENCES

1. P. Dhar, "The carbon impact of artificial intelligence," Nat. Mach. Intell. **2**, 423–425 (2020).
2. P. Fraga-Lamas, S. I. Lopes, and T. M. Fernández-Caramés, "Green IoT and edge AI as key technological enablers for a sustainable digital transition towards a smart circular economy: an industry 5.0 use case," Sensors **21**, 5745 (2021).
3. C. DeCusatis, "Optical Interconnects—Less Power to Them! (and why that's a good thing)," OFC, 2012, https://www.ofcconference.org/en-us/home/news-and-press/ofc-blog/2012/2012-september/optical-interconnects-%e2%80%93-less-power-to-them!-(and-w/.
4. Q. Cheng, M. Bahadori, M. Glick, *et al.*, "Recent advances in optical technologies for data centers: a review," Optica **5**, 1354–1370 (2018).
5. S. Y. Siew, B. Li, F. Gao, *et al.*, "Review of silicon photonics technology and platform development," J. Lightwave Technol. **39**, 4374–4389 (2021).
6. H. Sepehrian, A. Yekani, L. A. Rusch, *et al.*, "CMOS-photonics codesign of an integrated DAC-Less PAM-4 silicon photonic transmitter," IEEE Trans. Circuits Syst. I: Regul. Pap. **63**, 2158–2168 (2016).
7. K. Li, D. J. Thomson, S. Liu, *et al.*, "An integrated CMOS–silicon photonics transmitter with a 112 gigabaud transmission and picojoule per bit energy efficiency," Nat. Electron. **6**, 910–921 (2023).
8. J. Shi, M. Jin, T. Yang, *et al.*, "16-channel photonic–electric co-designed silicon transmitter with ultra-low power consumption," Photonics Res. **11**, 143–149 (2023).
9. Q. Liao, Y. Zhang, S. Ma, *et al.*, "A 50-Gb/s PAM-4 silicon-photonic transmitter incorporating lumped-segment MZM, distributed CMOS driver, and integrated CDR," IEEE J. Solid-State Circuits **57**, 767–780 (2022).
10. F. Iseini, M. Inac, A. Malignaggi, *et al.*, "Monolithically integrated opto-electronic transmitter based on segmented Mach-Zehnder modulator in EPIC 250 nm BiCMOS technology," in *IEEE 23rd Topical Meeting on Silicon Monolithic Integrated Circuits in RF Systems* (2023), pp. 51–54.
11. K. Kawahara and T. Baba, "DAC- and DSP-free optical transmitter based on triple-parallel Si Mach-Zehnder modulators," in *IEEE Silicon Photonics Conference (SiPhotonics)* (2024).
12. H. Li, G. Balamurugan, T. Kim, *et al.*, "A 3-D-integrated silicon photonic microring-based 112-Gb/s PAM-4 transmitter with nonlinear equalization and thermal control," IEEE J. Solid-State Circuits **56**, 19–29 (2021).
13. C. Sun, M. Wade, M. Georgas, *et al.*, "A 45 nm CMOS-SOI monolithic photonics platform with bit-statistics-based resonant microring thermal tuning," IEEE J. Solid-State Circuits **51**, 893–907 (2016).
14. H. Li, Z. Xuan, A. Titriku, *et al.*, "A 25 Gb/s, 4.4 V-swing, AC-coupled ring modulator-based WDM transmitter with wavelength stabilization in 65 nm CMOS," IEEE J. Solid-State Circuits **50**, 3145–3159 (2015).
15. D. M. Dourado, G. B. de Farias, R. H. Gounella, *et al.*, "Challenges in silicon photonics modulators for data center interconnect applications," Opt. Laser Technol. **144**, 107376 (2021).
16. S. Shekhar, W. Bogaerts, L. Chrostowski, *et al.*, "Roadmapping the next generation of silicon photonics," Nat. Commun. **15**, 751 (2024).
17. J. Müller, F. Merget, S. S. Azadeh, *et al.*, "Optical peaking enhancement in high-speed ring modulators," Sci. Rep. **4**, 6310 (2014).
18. J. Sun, R. Kumar, M. Sakib, *et al.*, "A 128 Gb/s PAM4 silicon microring modulator with integrated thermo-optic resonance tuning," J. Lightwave Technol. **37**, 110–115 (2019).
19. H. Cai, S. Fu, Y. Yu, *et al.*, "Lateral-zigzag PN junction enabled high-efficiency silicon micro-ring modulator working at 100 Gb/s," IEEE Photonics Technol. Lett. **34**, 525–528 (2022).
20. Y. Zhang, Y. Zhang, H. Zhang, *et al.*, "240 Gb/s optical transmission based on an ultrafast silicon microring modulator," Photonics Res. **10**, 1127–1133 (2022).
21. D. J. Thomson, F. Y. Gardes, J.-M. Fedeli, *et al.*, "50-Gb/s silicon optical modulator," IEEE Photonics Technol. Lett. **24**, 234–236 (2012).
22. G. Cong, M. Ohno, Y. Maegami, *et al.*, "Silicon traveling-wave Mach–Zehnder modulator under distributed-bias driving," Opt. Lett. **43**, 403–406 (2018).
23. M. Pantouvaki, S. A. Srinivasan, Y. Ban, *et al.*, "Active components for 50 Gb/s NRZ-OOK optical interconnects in a silicon photonics platform," J. Lightwave Technol. **35**, 631–638 (2017).
24. G. Cong, Y. Maegami, M. Ohno, *et al.*, "Ultra-compact non-travelling-wave silicon carrier-depletion Mach-Zehnder modulators towards high

channel density integration," IEEE J. Sel. Top. Quantum Electron. **27**, 1–11 (2021).
25. M. Li, L. Wang, X. Li, *et al.*, "Silicon intensity Mach–Zehnder modulator for single lane 100 Gb/s applications," Photonics Res. **6**, 109–116 (2018).
26. Y. Zhou, L. Zhou, H. Zhu, *et al.*, "Modeling and optimization of a single-drive push-pull silicon Mach-Zehnder modulator," Photonics Res. **4**, 153–161 (2016).
27. S. Menezo, T. Thiessen, P. Grosse, *et al.*, "High-speed heterogeneous InP-on-Si capacitive phase modulators," in *Optical Fiber Communications Conference and Exposition (OFC)* (2018), pp. 1–3.
28. J.-H. Han, M. Takenaka, and S. Takagi, "Extremely high modulation efficiency III-V/Si hybrid MOS optical modulator fabricated by direct wafer bonding," in *IEEE International Electron Devices Meeting (IEDM)* (2016), pp. 25.5.1–25.5.4.
29. G.-W. Lu, J. Hong, F. Qiu, *et al.*, "High-temperature-resistant silicon-polymer hybrid modulator operating at up to 200 Gbit s^{-1} for energy-efficient datacentres and harsh-environment applications," Nat. Commun. **11**, 4224 (2020).
30. H. Sato, J. Mao, A. Bannaron, *et al.*, "A 100 Gbaud on-off-keying silicon-polymer hybrid modulator operating at up to 110°C," IEEE Photonics Technol. Lett. **33**, 1507–1510 (2021).
31. V. Sorianello, G. Contestabile, and M. Romagnoli, "Graphene on silicon modulators," J. Lightwave Technol. **38**, 2782–2789 (2020).
32. X. Hu, Y. Zhang, D. Chen, *et al.*, "Design and modeling of high efficiency graphene intensity/phase modulator based on ultra-thin silicon strip waveguide," J. Lightwave Technol. **37**, 2284–2292 (2019).
33. C. Wang, M. Zhang, X. Chen, *et al.*, "Integrated lithium niobate electro-optic modulators operating at CMOS-compatible voltages," Nature **562**, 101–104 (2018).
34. F. Valdez, V. Mere, and S. Mookherjea, "100 GHz bandwidth, 1 volt integrated electro-optic Mach–Zehnder modulator at near-IR wavelengths," Optica **10**, 578–584 (2023).
35. G. Chen, K. Chen, J. Zhang, *et al.*, "Compact 100 GBaud driverless thin-film lithium niobate modulator on a silicon substrate," Opt. Express **30**, 25308–25317 (2022).
36. B. Pan, H. Cao, Y. Huang, *et al.*, "Compact electro-optic modulator on lithium niobate," Photonics Res. **10**, 697–702 (2022).
37. T. Baba, "Slow light in photonic crystals," Nat. Photonics **2**, 465–473 (2008).
38. H. C. Nguyen, Y. Sakai, M. Shinkawa, *et al.*, "Photonic crystal silicon optical modulators: carrier-injection and depletion at 10 Gb/s," IEEE J. Quantum Electron. **48**, 210–220 (2012).
39. Y. Hinakura, H. Arai, and T. Baba, "64 Gbps Si photonic crystal slow light modulator by electro-optic phase matching," Opt. Express **27**, 14321–14327 (2019).
40. Y. Hinakura, D. Akiyama, H. Ito, *et al.*, "Silicon photonic crystal modulators for high-speed transmission and wavelength division multiplexing," IEEE J. Sel. Top. Quantum Electron. **27**, 1–8 (2021).
41. D. M. Gill, W. M. J. Green, C. Xiong, *et al.*, "Distributed electrode Mach-Zehnder modulator with double-pass phase shifters and integrated inductors," Opt. Express **23**, 16857–16865 (2015).
42. K. Kawahara and T. Baba, "Modeling of Si rib and photonic crystal Mach-Zehnder modulators for electro-optic co-simulation up to 64 Gbaud," in *IEEE MTT-S International Conference on Numerical Electromagnetic and Multiphysics Modeling and Optimization (NEMO)* (2023), pp. 158–161.
43. N. Chen, B. Xiong, H. Yue, *et al.*, "High efficiency single-sideband modulator using coupled Bragg grating resonators on thin-film lithium niobate," in *Optical Fiber Communications Conference and Exhibition (OFC)* (2024).
44. G. Chen, K. Chen, R. Gan, *et al.*, "High performance thin-film lithium niobate modulator on a silicon substrate using periodic capacitively loaded traveling-wave electrode," APL Photonics **7**, 026103 (2022).
45. T. Tamura, K. Kondo, Y. Terada, *et al.*, "Silica-clad silicon photonic crystal waveguides for wideband dispersion-free slow light," J. Lightwave Technol. **33**, 3034–3040 (2015).
46. Y. Terada, T. Tatebe, Y. Hinakura, *et al.*, "Si photonic crystal slow-light modulators with periodic p–n junctions," J. Lightwave Technol. **35**, 1684–1692 (2017).
47. R. Shiratori, M. Nakata, K. Hayashim, *et al.*, "Particle swarm optimization of silicon photonic crystal waveguide transition," Opt. Lett. **46**, 1904–1907 (2021).
48. "GlobalFoundries 12 LP—CMC microsystems," https://www.cmc.ca/globalfoundries-12-lp/.
49. C. Han, Z. Zheng, H. Shu, *et al.*, "Slow-light silicon modulator with 110-GHz bandwidth," Sci. Adv. **9**, eadi5339 (2023).
50. H. Xu, X. Li, X. Xiao, *et al.*, "High-speed silicon modulator with band equalization," Opt. Lett. **39**, 4839–4842 (2014).
51. L. Breyne, J. Lambrecht, M. Verplaetse, *et al.*, "Electro-optic frequency response shaping using embedded FIR filters in slow-wave modulators," J. Lightwave Technol. **39**, 1777–1784 (2021).
52. M. Streshinsky, R. Ding, Y. Liu, *et al.*, "Low power 50 Gb/s silicon traveling wave Mach-Zehnder modulator near 1300 nm," Opt. Express **21**, 30350–30357 (2013).
53. R. Ding, Y. Liu, Q. Li, *et al.*, "Design and characterization of a 30-GHz bandwidth low-power silicon traveling-wave modulator," Opt. Commun. **321**, 124–133 (2014).
54. A. Brimont, D. J. Thomson, F. Y. Gardes, *et al.*, "Low drive voltage 10 Gb/s and high contrast 40 Gb/s silicon slow wave modulators," in *9th International Conference on Group IV Photonics (GFP)* (2012), pp. 195–197.
55. O. Jafari, W. Shi, and S. Larochelle, "Mach-Zehnder silicon photonic modulator assisted by phase-shifted Bragg gratings," IEEE Photonics Technol. Lett. **32**, 445–448 (2020).
56. J. Ding, H. Chen, L. Yang, *et al.*, "Ultra-low-power carrier-depletion Mach-Zehnder silicon optical modulator," Opt. Express **20**, 7081–7087 (2012).
57. Z. Yong, W. D. Sacher, Y. Huang, *et al.*, "U-shaped PN junctions for efficient silicon Mach-Zehnder and microring modulators in the O-band," Opt. Express **25**, 8425–8439 (2017).

175.177.6.12 {ts '2024-08-28 21:14:12'}